Pitaya-Inspired Metal-Organic Framework Nanozyme for Multimodal Imaging-Guided Synergistic Cuproptosis, Nanocatalytic Therapy, and Photothermal Therapy

Quer Yue, Qingbin Zeng, Qianni Guo,* Xiuchao Zhao, Yaping Yuan, Yuqi Yang, Weiping Jiang, and Xin Zhou*

Nature often provides invaluable insights into technological innovation and the construction of nanomaterials. Inspired by the pitaya fruit's strategy of wrapping seeds within its pulp to enhance seed survival, a unique nanocomposite based on metal-organic framework (MOF)-encapsulated CuS nanoparticles (NPs) is developed. This design effectively addresses the challenge of short retention time afforded by CuS NPs for therapeutic and imaging purposes. The MOF acts as the "pitaya pulp" protecting the internal CuS NPs ("pitaya seeds"), thereby increasing their retention time in vivo. This system exhibits triple-enzyme-mimicking activities and is proposed for application in photoacoustic and magnetic resonance imaging-guided therapies, including chemodynamic therapy, photothermal therapy, and cuproptosis-related therapy. The exceptional enzyme-mimicking activities of superoxide dismutase, catalase, and peroxidase not only produce oxygen to alleviate hypoxia but also generate a reactive oxygen species (ROS) storm for effective tumor destruction. By combining these multienzymatic properties, superior photothermal performance, and Cu-induced cuproptosis, nanozyme-treated mice exhibited an 84% inhibition of tumor growth—approximately double the effect observed in mice treated with CuS NPs alone. This study presents a smart strategy for integrating imaging with therapeutic modalities, achieving exceptional outcomes for precise imaging-guided tumor therapy.

1. Introduction

Copper plays a crucial role in cellular metabolic processes, serving as a cofactor in various enzymes and regulating cell signaling pathways.[1–4] However, abnormal copper levels can cause cytotoxicity and induce cell death via a newly identified pathway known as cuproptosis,[5–15] which is different from other forms of cell death such as pyroptosis,[16] apoptosis,[17] and ferroptosis.[9,12,18] In cuproptosis, copper ions bind to lipoylated proteins, particularly dihydrolipoamide S-acetyltransferase (DLAT) in the tricarboxylic acid (TCA) cycle. This binding triggers protein aggregation, loss of iron–sulfur (Fe-S) cluster proteins, and proteotoxic stress, ultimately leading to cell death.[19] Cuproptosis has emerged as a promising strategy for cancer treatment. However, effectively inducing cuproptosis in tumor cells remains challenging owing to variations in copper ion metabolism and the inconsistent efficacy of copper ionophores.

CuS is a commonly used inorganic material with significant potential as a cuproptosis agent for cancer therapy.[20] As important transition metal sulfides, CuS nanoparticles (NPs) exhibit stable properties and function as enzyme mimetics.[21–24] They can generate the activities of three types of enzyme activities, viz., peroxidase (POD), catalase (CAT), and superoxide dismutase (SOD), which increase the oxygen levels in the hypoxic tumor microenvironment and produce reactive oxygen species, thus promoting tumor elimination synergistically. Additionally, CuS NPs exhibit strong near-infrared light absorption and high photothermal conversion efficiency, making them ideal for applications in photoacoustic imaging (PAI),[25] photothermal imaging (PTI), and photothermal therapy (PTT).[26–30] However, directly using CuS NPs as imaging and therapeutic agents presents challenges owing to their small particle size, which can lead to sub-optimal imaging and therapeutic outcomes. Combining CuS NPs with other platforms is a promising approach to improving both the retention time and enhanced permeability and retention (EPR) effect, leading to better imaging and therapeutic efficacy.

Q. Yue, Q. Zeng, Q. Guo, X. Zhao, Y. Yuan, Y. Yang, W. Jiang, X. Zhou
State Key Laboratory of Magnetic Resonance and Atomic and Molecular Physics
National Center for Magnetic Resonance in Wuhan
Wuhan Institute of Physics and Mathematics
Innovation Academy for Precision Measurement Science and Technology
Chinese Academy of Sciences
Wuhan 430071, P. R. China
E-mail: qian-niguo@wipm.ac.cn; xinzhou@wipm.ac.cn
Q. Yue, Q. Zeng, Q. Guo, X. Zhao, Y. Yuan, Y. Yang, W. Jiang, X. Zhou
University of Chinese Academy of Sciences
Beijing 100049, P. R. China
X. Zhou
School of Biomedical Engineering
Hainan University
Haikou 570228, P. R. China

The ORCID identification number(s) for the author(s) of this article can be found under https://doi.org/10.1002/adhm.202402915
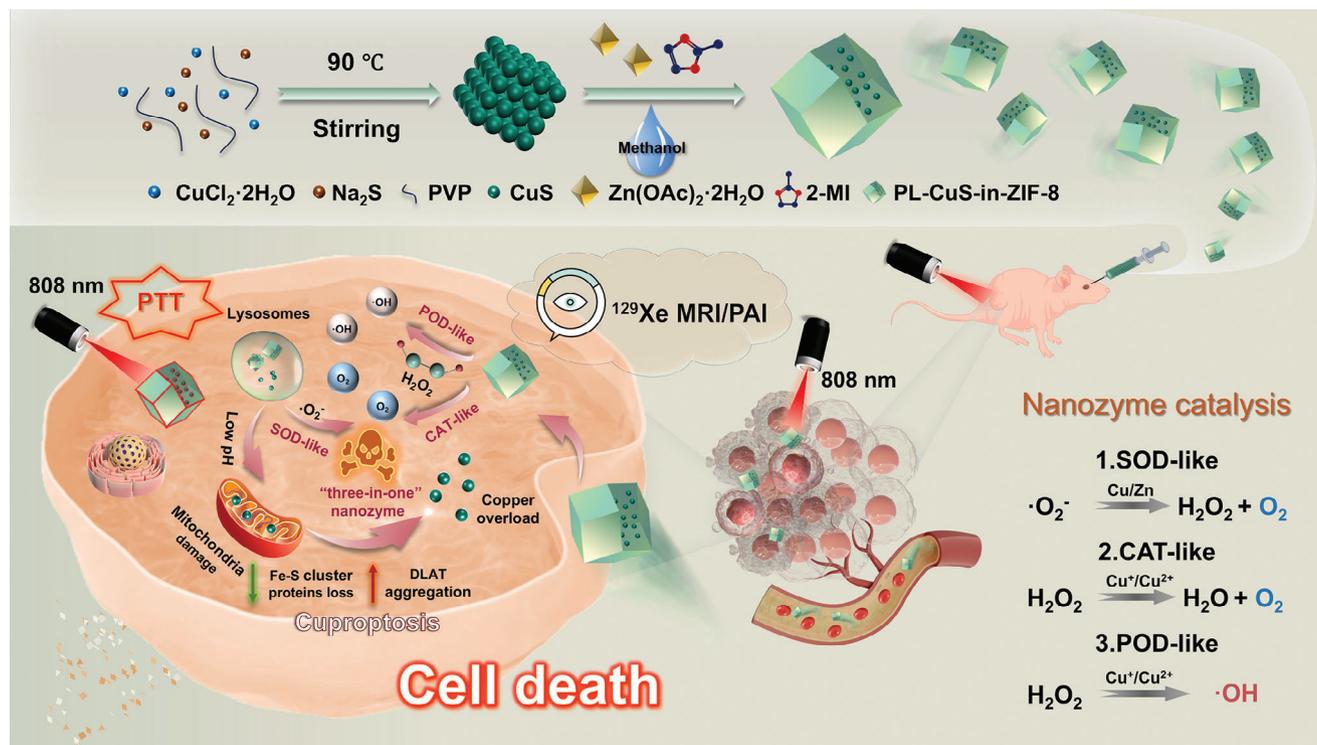
Scheme 1. Schematic illustration of multimodal imaging-guided tumor therapy by using PL-CuS-in-ZIF-8. Following intravenous administration, PL-CuS-in-ZIF-8 accumulates at tumor sites, where it releases CuS. The released CuS induces cuproptosis and multienzymatic activity at the tumor site, while its excellent photothermal performance enhances the antitumor efficacy.

Metal-organic frameworks (MOFs) are crystalline materials renowned for their regular porosity, substantial pore volume, and versatile structural and functional properties.[31–37] The incorporation of NPs into MOFs has gained considerable attention owing to the unique chemical and physical properties exhibited by these NPs.[38–40] Additionally, certain MOFs can serve as contrast agents for magnetic resonance imaging (MRI). For instance, the water-stable metal-organic framework (MOF), viz., ZIF-8, demonstrates the ability to entrap xenon atoms for hyperpolarized ^{129}Xe MRI,[41,42] offering heightened sensitivity for detecting trace molecules at picomolar concentrations. However, relying on a single imaging strategy has limitations, such as the inability to provide comprehensive information about the disease.

Natural and real-world examples often inspire innovative solutions. Drawing from these sources, we developed a unique nanocomposite structure, modeled after the pitaya fruit, based on ZIF-8-encapsulated CuS NPs, referred to as PL-CuS-in-ZIF-8. In this design, ZIF-8 acts as the protective "pitaya pulp," whereas CuS NPs serve as the "pitaya seeds." Similar to how the pitaya fruit's pulp protects its seeds from external impacts, preserving their functionality, ZIF-8 encapsulates the CuS NPs, protecting them from external influences and potentially improving their retention time and efficacy. This versatile platform not only exhibits triple-enzyme-mimicking activities and cuproptosis therapy potential but also enables hyperpolarized ^{129}Xe MRI, PAI, and PTT capabilities.

Upon internalization by cells, PL-CuS-in-ZIF-8 releases CuS, which exhibits CAT-like and POD-like activities upon interaction with tumoral H_2O_2, generating O_2 and $\cdot$OH, respectively.

Moreover, its SOD-like activity scavenges $\cdot O^{2-}$ to generate O_2 and H_2O_2, facilitating multi-channel chemodynamic therapy (CDT). Additionally, CuS-mediated cuproptosis and thermal energy from the photothermal effect induce apoptosis in tumor cells. The combination of nanocatalytic therapy with cuproptosis and PTT enhances the overall effectiveness of tumor treatment (**Scheme 1**). This paper presents a promising multimodal imaging-guided tumor therapy and paves the way for developing cancer treatments based on cuproptosis and nanocatalytic therapy.

2. Results and Discussion

2.1. Synthesis and Characterization of Various NPs

Morphology plays a crucial role in determining the properties of nanomaterials. To investigate the impact of morphology on the imaging ability and xenon entrapment capability of MOF composites, various MOF composites were constructed by altering the type of zinc salts, 2-MI/Zn^{2+} ratio, and the mixing method of CuS NPs. The nanocomposites were classified into three groups based on the location of the CuS NPs: (I) a large number of CuS NPs encapsulated in ZIF-8, forming a pitaya-like nanocomposite (denoted as PL-CuS-in-ZIF-8); (II) CuS NPs loaded on the ZIF-8 surface, creating a strawberry-like nanocomposite (denoted as SL-CuS-on-ZIF-8); and (III) a small number of CuS NPs encapsulated in ZIF-8, producing a cherry-like nanocomposite (denoted as CL-CuS-in-ZIF-8). Transmission electron microscopy (TEM) images revealed that the CuS NPs are ≈10 nm in size, with a

**ADVANCED
SCIENCE NEWS**

www.advancedsciencenews.com

**ADVANCED
HEALTHCARE
MATERIALS**

www.advhealthmat.de

lattice spacing of 0.393 nm (Figure S1, Supporting Information). Based on TEM images, the sizes of PL-CuS-in-ZIF-8 and SL-CuS-on-ZIF-8 are ≈250 nm, whereas that of CL-CuS-in-ZIF-8 is ≈20 nm. TEM, scanning electron microscopy (SEM), and high-angle annular dark-field scanning transmission electron microscopy images (**Figure 1a**) demonstrated that PL-CuS-in-ZIF-8 contains a large number of CuS NPs inside, whereas CL-CuS-in-ZIF-8 has only a few entrapped CuS NPs. Additionally, both PL-CuS-in-ZIF-8 and CL-CuS-in-ZIF-8 exhibit smooth surfaces without any CuS NPs attached externally. In contrast, SL-CuS-on-ZIF-8 NPs had a large number of CuS NPs attached to the surface of ZIF-8 (Figure 1a). Elemental mapping and energy-dispersive X-ray spectroscopy (EDX) confirmed that CuS NPs were encapsulated within CL-CuS-in-ZIF-8 and PL-CuS-in-ZIF-8, whereas they remained attached to the surface of SL-CuS-on-ZIF-8 (Figure 1a; Figures S2–S5, Supporting Information). The CuS NPs exhibited a negative zeta potential of ≈−5.4 mV, whereas SL-CuS-on-ZIF-8, CL-CuS-in-ZIF-8, ZIF-8, and PL-CuS-in-ZIF-8 exhibited positive zeta potentials of 9.1, 18.1, 27.7, and 32.9 mV, respectively (Figure 1b). Powder X-ray diffraction (PXRD) patterns of these nanocomposites aligned well with those of pristine ZIF-8 NPs and the simulation (Figure 1c), indicating good phase purity and crystallinity. The lattice structure of ZIF-8 crystals remained unchanged even after the incorporation of CuS NPs.

The UV–vis spectra of the NPs showed broad absorption over the wavelength range of 700–1100 nm, which is characteristic of CuS NPs. For PL-CuS-in-ZIF-8, the absorption profile mirrored that of CuS NPs, whereas SL-CuS-on-ZIF-8 and CL-CuS-on-ZIF-8 displayed weaker absorption, likely due to poor dispersion (Figure 1d). The CuS loading percentages, determined using inductively coupled plasma mass spectrometry, were 2.04%, 1.71%, and 3.19% for PL-CuS-in-ZIF-8, SL-CuS-on-ZIF-8, and CL-CuS-on-ZIF-8, respectively (Table S1, Supporting Information). The formation process of PL-CuS-in-ZIF-8 NPs was illustrated by TEM. The CuS NPs act as seed crystals, and the ZIF-8 NPs grow on the surface of CuS, ultimately forming larger nanospheres (Figure S6, Supporting Information). We further explored the release profile of CuS from PL-CuS-in-ZIF-8 in a mildly acidic environment. TEM imaging after dispersing PL-CuS-in-ZIF-8 in a HOAc-NaOAc buffer solution (pH 5.5) revealed that the NPs disintegrated after 1 h, with CuS NPs dominating after 2 h (Figures S7A–D, Supporting Information). UV–vis spectra also indicated the release of CuS NPs from PL-CuS-in-ZIF-8 (Figure S7E, Supporting Information).

X-ray photoelectron spectroscopy was used to analyze the modification of PL-CuS-in-ZIF-8 (Figure S8, Supporting Information). Cu $2p_{1/2}$ binding energies were observed to be 952.7 eV for Cu$^+$ and 954.1 eV for Cu^{2+}, and Cu $2p_{3/2}$ binding energies were found to be 933.0 eV for Cu$^+$ and 934.3 eV for Cu^{2+}, along with a satellite peak at 945.6 eV. This indicates stable incorporation of CuS NPs within the ZIF-8 structure.

Thermogravimetric analysis (TGA) showed no weight loss before 400 °C (Figure 1e), confirming the high thermal stability of the materials and the complete removal of solvent molecules from the MOF pores. Interestingly, the thermal degradation temperature of the SL-CuS-on-ZIF-8 composite is significantly higher than that of the other composites. This enhancement is likely due to the presence of CuS NPs on the ZIF-8 surface, which could raise the thermal degradation temperature of ZIF-8.

N$_2$ adsorption experiments were conducted to evaluate the permanent porosity of these composites (Figures S9–S12, Supporting Information). The Brunauer–Emmett–Teller surface area of PL-CuS-in-ZIF-8 was ≈1785 m^2 g^{-1}, surpassing those of pristine ZIF-8 (1314 m^2 g^{-1}), CL-CuS-in-ZIF-8 (1463 m^2 g^{-1}), and SL-CuS-on-ZIF-8 (1679 m^2 g^{-1}) NPs. CL-CuS-in-ZIF-8 composites exhibited a distinct distribution peak near 10 nm, suggesting the formation of a mesoporous structure within, whereas PL-CuS-in-ZIF-8 showed no mesoporosity.

When SL-CuS-on-ZIF-8, CL-CuS-in-ZIF-8, and PL-CuS-in-ZIF-8 were dispersed in water at identical concentrations, all three displayed the Tyndall effect (Figures S13a and S14a, Supporting Information). However, after standing for two days, SL-CuS-on-ZIF-8 and CL-CuS-in-ZIF-8 exhibited settling, whereas PL-CuS-in-ZIF-8 remained uniformly dispersed and continued to show the Tyndall effect (Figures S13b and S14b, Supporting Information).

2.2. In Vitro Testing of PL-CuS-in-ZIF-8 Functions

Solvent-free composites, including pristine ZIF-8, SL-CuS-on-ZIF-8, CL-CuS-in-ZIF-8, and PL-CuS-in-ZIF-8, were assessed for their ability to trap xenon using hyperpolarized ^{129}Xe NMR spectroscopy. The composites were dispersed in aqueous solution, and ^{129}Xe NMR spectra were obtained. All samples exhibited two characteristic peaks in aqueous solution with 5 mg mL^{-1} NPs: one peak at 193 ppm, attributed to dissolved ^{129}Xe, and another peak near 83 ppm, corresponding to ^{129}Xe entrapped within the pores of the composites (**Figure 2a**). Significant differences were observed in the entrapped ^{129}Xe chemical shift, signal intensity, and full width at half maximum (FWHM) among the materials (Table S2, Supporting Information). The smaller particle size of CL-CuS-in-ZIF-8 resulted in lower entrapped ^{129}Xe signal intensity and narrower FWHM than those of materials with larger particle sizes, which is consistent with our previous findings.[42] For SL-CuS-on-ZIF-8, the surface-adsorbed CuS NPs negatively impacted xenon entrapment capacity, resulting in the weakest entrapped ^{129}Xe NMR signal intensity. In contrast, PL-CuS-in-ZIF-8 exhibited the strongest entrapped ^{129}Xe NMR signal intensity among the materials tested. With respect to pristine ZIF-8, PL-CuS-in-ZIF-8 showed comparable ^{129}Xe signal intensity (Figure 2a; Table S2, Supporting Information). Considering the entrapped ^{129}Xe NMR signal intensity, nanocomposite morphology, CuS NPs encapsulation efficiency, and stability, PL-CuS-in-ZIF-8 is identified as the optimal nanocomposite.

Owing to the excellent photothermal conversion properties of CuS NPs, the stability of PL-CuS-in-ZIF-8 was evaluated using TEM and ^{129}Xe NMR spectroscopy after exposure to near-infrared (NIR) laser irradiation. PL-CuS-in-ZIF-8 NPs were dispersed in an aqueous solution and irradiated with an 808 nm NIR laser at an intensity of 1 W cm^{-2} for 5 min. TEM images revealed that laser irradiation did not alter the morphology of the NPs. Moreover, the entrapped ^{129}Xe NMR signal intensity and chemical shift remained unchanged post-irradiation (Figure S15; Table S3, Supporting Information), indicating that the laser treatment did not cause deformation or degradation of PL-CuS-in-ZIF-8, demonstrating its high photothermal stability compared to that of previously reported systems.[30]
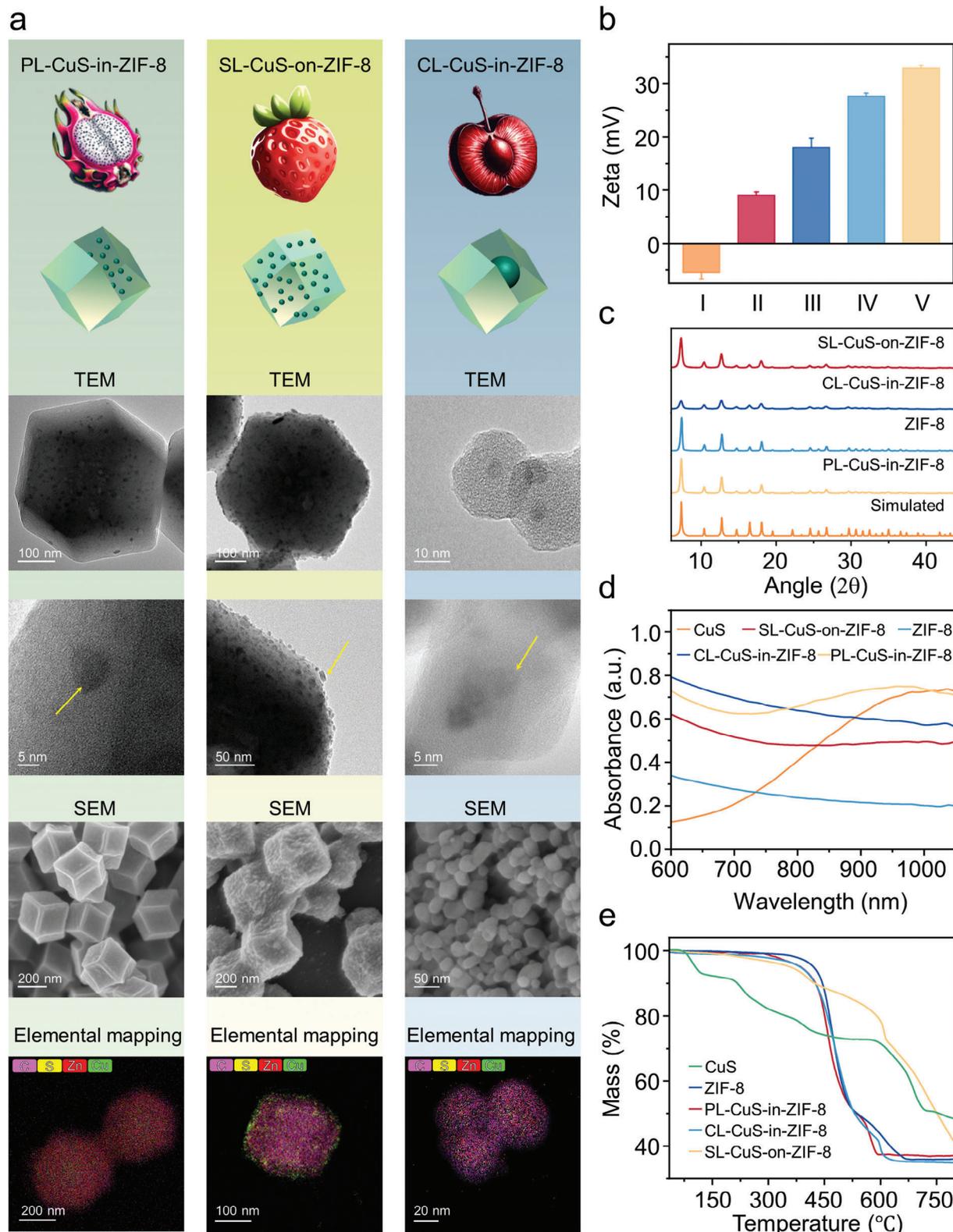
**ADVANCED
SCIENCE NEWS**

www.advancedsciencenews.com

**ADVANCED
HEALTHCARE
MATERIALS**

www.advhealthmat.de

Figure 1. a) TEM and SEM images of PL-CuS-in-ZIF-8, SL-CuS-on-ZIF-8, and CL-CuS-in-ZIF-8. b) Zeta potential of the NPs: I: CuS, II: SL-CuS-on-ZIF-8, III: CL-CuS-in-ZIF-8, IV: ZIF-8, V: PL-CuS-in-ZIF-8. Data are presented as mean ± SD, n = 3. c) PXRD patterns of SL-CuS-on-ZIF-8, CL-CuS-in-ZIF-8, ZIF-8, and PL-CuS-in-ZIF-8. d) UV–vis spectra of CuS, SL-CuS-on-ZIF-8, CL-CuS-in-ZIF-8, ZIF-8, and PL-CuS-in-ZIF-8. e) TGA curves of CuS, SL-CuS-on-ZIF-8, CL-CuS-in-ZIF-8, ZIF-8, and PL-CuS-in-ZIF-8.
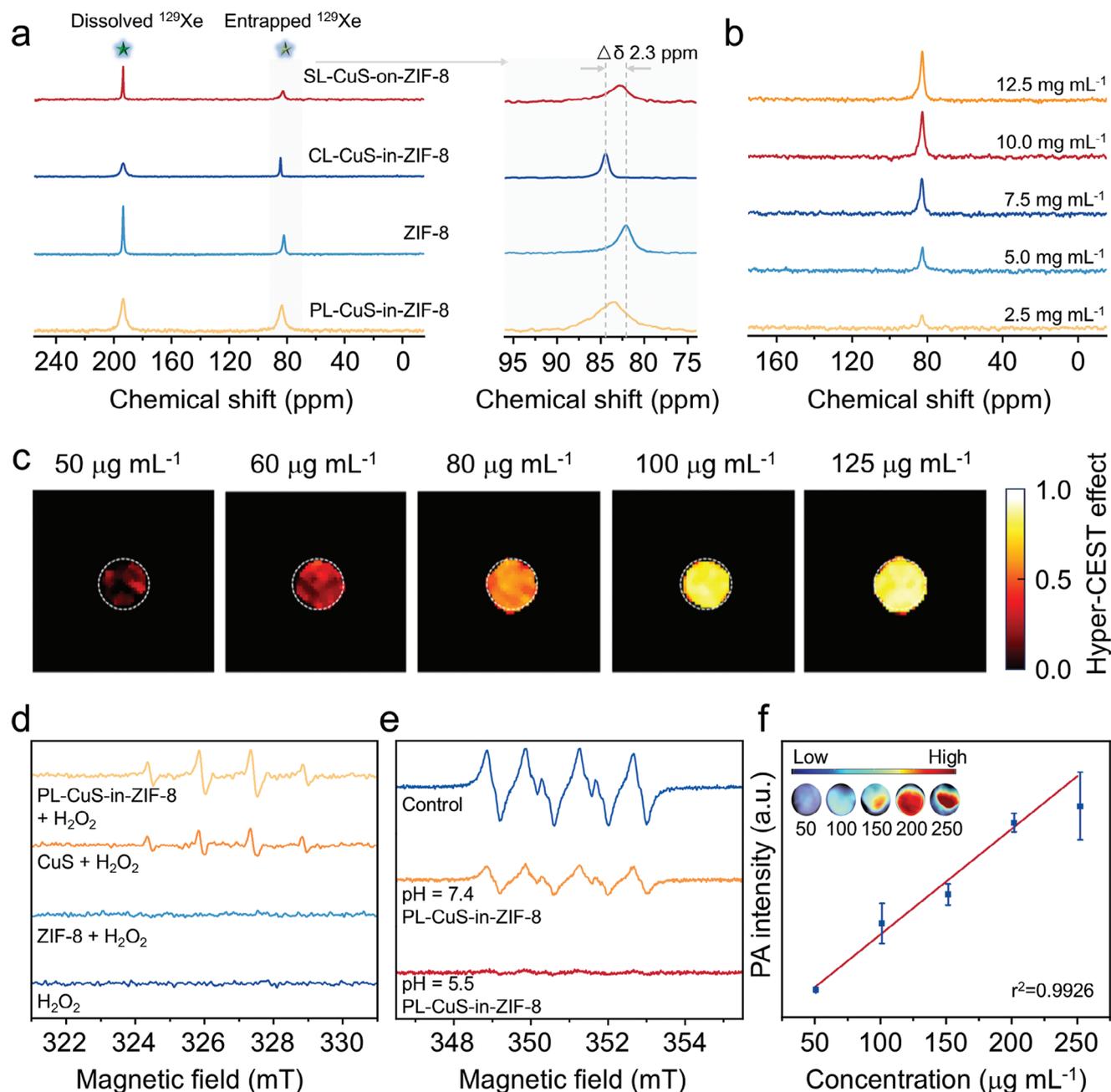
**ADVANCED
SCIENCE NEWS**

www.advancedsciencenews.com

**ADVANCED
HEALTHCARE
MATERIALS**

www.advhealthmat.de

Figure 2. a) Hyperpolarized ^{129}Xe NMR spectra of SL-CuS-on-ZIF-8, CL-CuS-in-ZIF-8, ZIF-8, and PL-CuS-in-ZIF-8 at a concentration of 5 mg mL^{-1}. b) Hyperpolarized ^{129}Xe NMR spectra recorded for aqueous solutions of PL-CuS-in-ZIF-8 at different concentrations (2.5, 5.0, 7.5, 10.0, and 12.5 mg mL^{-1}). c) Hyper-CEST MRI of PL-CuS-in-ZIF-8 at different concentrations (50, 60, 80, 100, and 125 mg mL^{-1}) in aqueous solution. d) ESR spectrum detecting hydroxyl radicals using DMPO as a trapping agent. e) ESR spectrum detecting superoxide radicals using BMPO as a trapping agent. f) PA imaging of different concentrations of PL-CuS-in-ZIF-8. Data are shown as mean ± SD, n = 3.

A series of PL-CuS-in-ZIF-8 NPs were prepared to examine the impact of CuS NPs loading on the entrapped ^{129}Xe signal intensity. Varying initial quantities of CuS NPs (10, 15, 20, 25, and 30 mg) were added to the reaction solution. Although the initial quantity of CuS NPs did not significantly affect the CuS loading ratio (Table S4, Supporting Information), it influenced the particle size of the nanocomposites and the entrapped ^{129}Xe NMR signal intensity. PL-CuS-in-ZIF-8 constructed with 15 mg CuS NPs yielded the optimal signal intensity (Figure S16; Table S5, Supporting Information). The entrapped ^{129}Xe NMR signal intensity increased with the concentration of PL-CuS-in-ZIF-8 in solution, whereas the chemical shift remained constant. A linear relationship between the entrapped ^{129}Xe NMR signal intensity and PL-CuS-in-ZIF-8 concentration was established in the concentration range of 2.5–12.5 mg mL^{-1} (Figure 2b; Table S6, Supporting Information).

**ADVANCED
SCIENCE NEWS**

www.advancedsciencenews.com

**ADVANCED
HEALTHCARE
MATERIALS**

www.advhealthmat.de

Furthermore, hyperpolarized xenon chemical exchange saturation transfer (Hyper-CEST) was employed to further assess the xenon entrapment capability of PL-CuS-in-ZIF-8 at low concentrations (Figure S17, Supporting Information). PL-CuS-in-ZIF-8 displayed two distinct saturation responses, with dissolved ^{129}Xe and entrapped ^{129}Xe showing peak positions at 193 and 84 ppm, respectively. Even at a low concentration of PL-CuS-in-ZIF-8 (50 µg mL^{-1}), the Hyper-CEST effect was ≈39%, indicating excellent xenon entrapment capability at ultralow concentrations. When the concentration of PL-CuS-in-ZIF-8 increased to 125 µg mL^{-1}, almost 100% saturation response was observed at 84 ppm. Additionally, the Hyper-CEST effect exhibited a polynomial relationship over the concentration range of 50–125 µg mL^{-1} (Figure S18, Supporting Information). Hyper-CEST MRI at various concentrations of PL-CuS-in-ZIF-8 in aqueous solution revealed strong signal intensity (Figure 2c), the MRI signal intensity showed a polynomial relationship with the concentration of PL-CuS-in-ZIF-8 (Figure S19, Supporting Information). These findings highlight the remarkable xenon entrapment capability of PL-CuS-in-ZIF-8, making it an ideal xenon host.

The multienzyme-like activity of PL-CuS-in-ZIF-8 was evaluated. The abundant H_2O_2 in tumors can be catalyzed to ·OH by a POD-like enzyme for CDT of tumors. First, the POD-like activity of PL-CuS-in-ZIF-8 was monitored using electron spin resonance (ESR); 5,5-dimethyl-1-pyrroline N-oxide (DMPO) was employed to trap the ·OH species. The typical quadruple peak pattern (1:2:2:1) observed in DMPO-trapped ·OH species confirmed the generation of ·OH by PL-CuS-in-ZIF-8 in the presence of H_2O_2 (Figure 2d). ·OH generation was further analyzed by a colorimetric method using a 3,3′,5,5′-tetramethylbenzidine (TMB) assay. The absorbance of oxidized TMB at 652 nm rapidly increased when PL-CuS-in-ZIF-8 was present at pH 4.0, indicating effective production of ·OH in an acidic environment with H_2O_2 (Figure S20, Supporting Information). These results confirm the POD-like catalytic activity of PL-CuS-in-ZIF-8.

Furthermore, the SOD-like activity of PL-CuS-in-ZIF-8 was evaluated using ESR with the specific spin-trap reagent 5-tert-butoxycarbonyl-5-methyl-1-pyrroline-N-oxide (BMPO). The characteristic quadruple peak pattern (1:1:1:1) observed for BMPO-OOH confirmed the production of ·O_2^- by the xanthine and xanthine oxidase system. When PL-CuS-in-ZIF-8 NPs were present in the solution (pH 7.4), the signal intensity of the quadruple peak decreased significantly. Additionally, the quadruple peak completely disappeared when the solution pH was 5.5 (Figure 2e). These results confirm the clearance of ·O_2^- by PL-CuS-in-ZIF-8, indicating its SOD-like activity. The SOD-like activity was also assessed using a nitro-blue tetrazolium assay, where the absorbance and color of the solution gradually decreased with increasing concentrations of PL-CuS-in-ZIF-8 (Figure S21, Supporting Information). These results indicate the effective SOD-like activity exhibited by PL-CuS-in-ZIF-8 NPs.

Subsequently, the CAT-like activity of PL-CuS-in-ZIF-8 was determined using a dissolved oxygen meter. PL-CuS-in-ZIF-8 was dispersed in aqueous solutions at different concentrations, with H_2O_2 at a constant concentration (60 mM), and the oxygen content was measured using the dissolved oxygen meter. The production of O_2 gas was observed upon mixing PL-CuS-in-ZIF-8 with H_2O_2 (60 mM), and its concentration increased over time

(Figure S22, Supporting Information). These results confirm that PL-CuS-in-ZIF-8 NPs possess CAT-like activity.

These findings confirm that PL-CuS-in-ZIF-8 exhibits excellent multienzyme activities, functioning as a POD-like, SOD-like, and CAT-like enzyme. These enzymatic properties enable PL-CuS-in-ZIF-8 to supply O_2, alleviate hypoxic conditions within the tumor microenvironment, and generate sufficient amounts of reactive oxygen species (ROS) to disrupt the tumor's reductive and microenvironment defense mechanisms. This, in turn, facilitates effective tumor eradication.

Furthermore, the photothermal properties of PL-CuS-in-ZIF-8 were investigated. PL-CuS-in-ZIF-8 demonstrated a strong photothermal effect upon irradiation with an 808 nm laser. The temperature of the PL-CuS-in-ZIF-8 solution ($C_{CuS} = 40$ µg mL^{-1}) increased by 30 °C after irradiation with a power density of 2 W cm^{-2} for 300 s, whereas pristine ZIF-8 showed only a slight temperature increase under the same conditions (Figures S23 and S24, Supporting Information). The photothermal conversion rate of PL-CuS-in-ZIF-8 was calculated to be 60% using a previously reported method[43] (Figures S25 and S26, Supporting Information), indicating excellent photothermal conversion performance. When the PL-CuS-in-ZIF-8 aqueous solution ($C_{CuS} = 40$ µg mL^{-1}) was exposed to varying power densities (0.5, 1, 1.5, and 2 W cm^{-2}), the temperature of the solution increased significantly (Figure S27, Supporting Information). Additionally, PL-CuS-in-ZIF-8 demonstrated excellent photostability under 808 nm laser irradiation at a power density of 2 W cm^{-2} for 5 min, even after undergoing five heating-cooling cycles (Figure S28, Supporting Information). The photothermal effect of PL-CuS-in-ZIF-8 at various concentrations (C_{CuS} 5–40 µg mL^{-1}) was investigated under constant irradiation at 2 W cm^{-2}, and the temperature of the solution exhibited a direct correlation with concentration (Figure S29, Supporting Information).

To assess the feasibility of in vivo PAI, initial in vitro experiments were conducted to detect the photoacoustic (PA) signal of the PL-CuS-in-ZIF-8 solution. As anticipated, the PL-CuS-in-ZIF-8 NPs exhibited remarkable PA signals, with signal intensities being linearly proportional to the NPs concentrations (Figure 2f).

2.3. Cancer Cell Interference by PL-CuS-in-ZIF-8

To investigate the cellular uptake of PL-CuS-in-ZIF-8 NPs, cellular Hyper-CEST experiments were performed. After incubating A549 cells with PL-CuS-in-ZIF-8 NPs for 2 h, the cellular Hyper-CEST spectrum exhibited two saturation responses. The peak at ≈84 ppm corresponded to the ^{129}Xe entrapped by PL-CuS-in-ZIF-8 in solution, whereas the peak at ≈92 ppm indicated the entrapped ^{129}Xe within the cells (**Figure 3a**). Hyper-CEST MRI of the cells also showed a strong CEST effect (Figure 3b). Bio-TEM images confirmed the presence of PL-CuS-in-ZIF-8 in the cytoplasm, demonstrating efficient cellular uptake of the NPs (Figure 3c). Additionally, cellular uptake was examined using the Zn^{2+}-specific probe [N-(6-Methoxy-8-quinolyl)-p-toluenesulfonamide] (TSQ). The fluorescence intensity of TSQ within the cells increased over time (Figure S30, Supporting Information), indicating both uptake of PL-CuS-in-ZIF-8 and progressive release of Zn^{2+} ions into the cellular environment. These
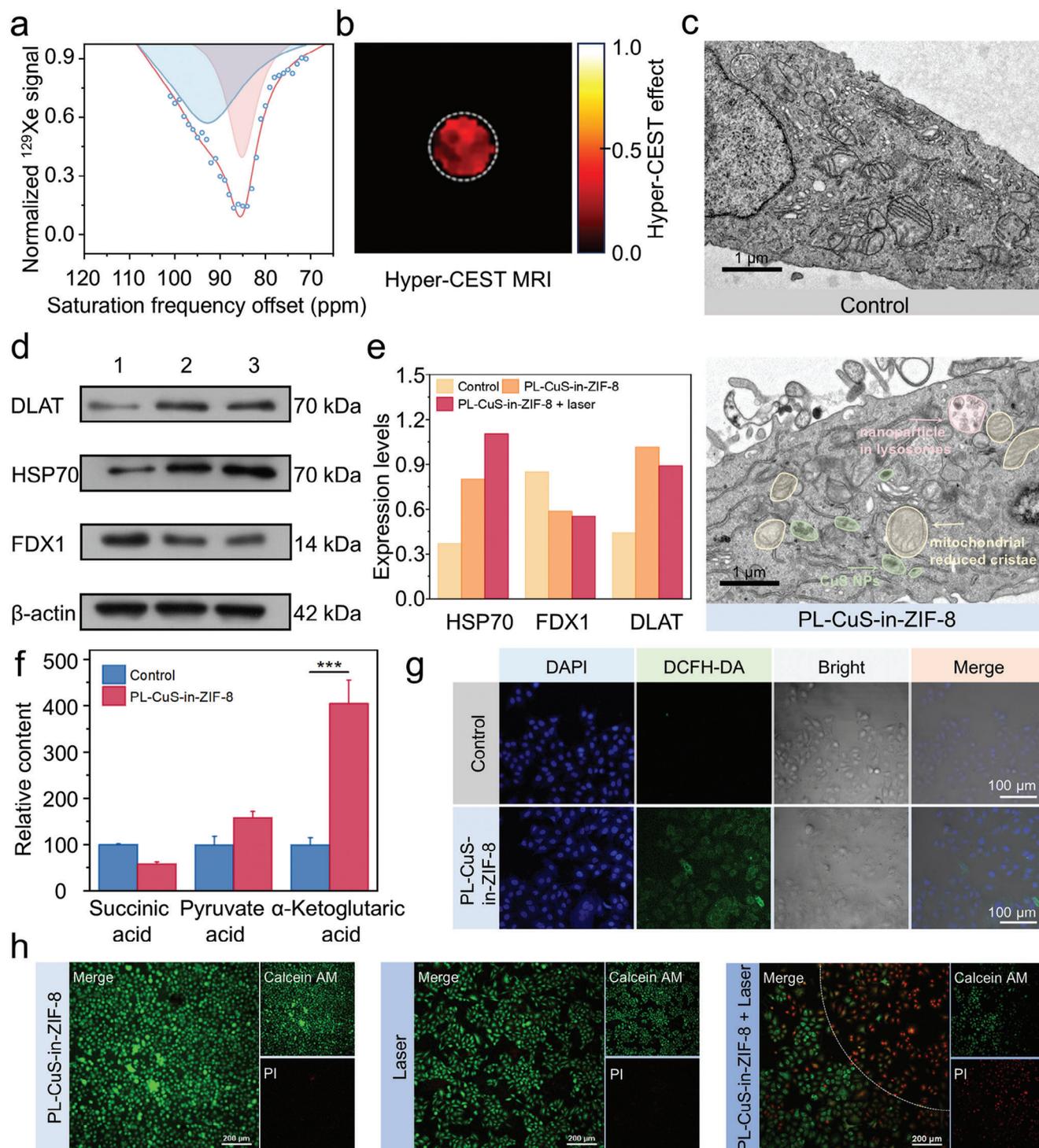
Figure 3. a) Hyper-CEST spectrum following co-incubation of 100 mg mL^{-1} PL-CuS-in-ZIF-8 with A549 cells for 2 h. b) Hyper-CEST MRI results after co-incubation of 100 mg mL^{-1} PL-CuS-in-ZIF-8 with A549 cells for 2 h. c) Bio-TEM images of A549 cells, control, and treatment (Scale bar = 1 µm). d) Western blot analysis of DLAT, HSP70, and FDX1 proteins in A549 cells after different treatments (1: control, 2: PL-CuS-in-ZIF-8, 3: PL-CuS-in-ZIF-8 + 808 nm laser). e) Quantitative analysis of western blot results. f) Detection of succinic acid, pyruvate, and α-ketoglutaric acid in A549 cells after different treatments using assay kits. Data are shown as mean ± SD, n = 3. g) ROS production in A549 cells with different treatments (Scale bar = 100 µm). h) Calcein-AM/PI co-stained A549 cells treated with PL-CuS-in-ZIF-8 under 808 nm laser irradiation for 5 min. ***$p < 0.001$.

**ADVANCED
SCIENCE NEWS**

www.advancedsciencenews.com

**ADVANCED
HEALTHCARE
MATERIALS**

www.advhealthmat.de

results confirm the efficient uptake of PL-CuS-in-ZIF-8 NPs by cells.

Cytotoxicity was assessed using the cell counting kit-8 assay. At high concentrations (200 μg mL^{-1}), PL-CuS-in-ZIF-8 showed minimal cytotoxic effects on human normal lung cells (BEAS-2B), with relative cell viability remaining at 90% (Figure S31b, Supporting Information). In contrast, it exhibited cytotoxic effects on human lung cancer cells (A549) at lower concentrations (120 μg mL^{-1}), resulting in a decrease in relative cell viability (<70%) (Figure S31a, Supporting Information), with a calculated IC50 value of 150 μg mL^{-1} (Figure S32, Supporting Information).

Based on bio-TEM analysis, the mitochondria of cells treated with PL-CuS-in-ZIF-8 exhibited reduced cristae compared to that of the control group, suggesting potential cuproptosis (Figure 3c). To confirm the role of cuproptosis in PL-CuS-in-ZIF-8 induced cell death, additional western blot assays were conducted to assess other hallmarks of cuproptosis (Figure 3d,e). The significant down-regulation of Fe-S cluster proteins (FDX1), along with the up-regulation of DLAT and HSP70 levels, indicated that PL-CuS-in-ZIF-8 effectively induces cuproptosis leading to cell death. Furthermore, after incubating A549 cells with PL-CuS-in-ZIF-8 NPs for 2 h, the levels of pyruvate and α-ketoglutaric acid in the TCA cycle increased by 58% and 405%, respectively, whereas succinic acid content decreased by 42% compared to that for the control group (Figure 3f). Primary morphological features indicative of cuproptosis included mitochondrial shrinkage and endoplasmic reticulum enlargement.[44] Confocal laser scanning microscopy analysis demonstrated increased endoplasmic reticulum fluorescence and decreased mitochondrial fluorescence in A549 cells treated with PL-CuS-in-ZIF-8 compared to that for the control group (Figure S33, Supporting Information). These results strongly support the conclusion that PL-CuS-in-ZIF-8 effectively induces cuproptosis.[8]

The generation of ROS at the cellular level was assessed using 2′,7′-dichlorofluorescein diacetate (DCFH-DA). In the presence of ROS, DCFH-DA undergoes oxidation and emits green fluorescence. Compared to the control group, cells treated with PL-CuS-in-ZIF-8 NPs exhibited prominent green fluorescence (Figure 3g), indicating that PL-CuS-in-ZIF-8 rapidly enhances intracellular ROS levels through a POD-like reaction with H$_2$O$_2$. The integrity of lysosomal membranes in A549 cells, following incubation with PL-CuS-in-ZIF-8 NPs, was assessed using the acridine orange (AO) staining method. AO emits green fluorescence in the cytoplasm and nuclei but shifts to red fluorescence when it accumulates in acidic organelles, particularly intact lysosomes. In untreated control cells, both red and green fluorescence were observed (Figures S34 and S35, Supporting Information). However, upon treatment with PL-CuS-in-ZIF-8 NPs, the red fluorescence significantly decreased, indicating lysosomal damage.[45] This effect is attributed to acid-triggered ·OH generation by PL-CuS-in-ZIF-8 NPs within endo/lysosomes. Lysosomal membrane permeabilization due to the loss of membrane integrity allows the release of lysosomal cathepsins into the cytosol, leading to cancer cell apoptosis. Consequently, a key mechanism of PL-CuS-in-ZIF-8 NPs-mediated cancer cell death involves lysosomal disruption through ·OH generation. Additionally, the cytotoxicity of PL-CuS-in-ZIF-8 was assessed using calcein AM and propidium iodide (PI) co-staining assays. Both the PL-CuS-in-ZIF-8 and laser groups exhibited strong green fluorescence, in-

dicating good biocompatibility of PL-CuS-in-ZIF-8 (Figure 3h). In contrast, the PL-CuS-in-ZIF-8 + 808 nm laser group exhibited the strongest red fluorescence in the laser-radiated area, accompanied by a significant decrease in green fluorescence, illustrating the superior anticancer efficacy of PL-CuS-in-ZIF-8 NPs. Additionally, flow cytometry analysis using the Annexin V-FITC/PI apoptosis detection assay demonstrated a higher percentage of apoptotic cancer cells in the PL-CuS-in-ZIF-8 + 808 nm laser group compared to other groups (Figure S36, Supporting Information). These results further validate the cancer treatment potential of PL-CuS-in-ZIF-8 NPs.

2.4. In Vivo Antitumor Efficacy

Hemolysis assays of PL-CuS-in-ZIF-8 demonstrated high biocompatibility, even at elevated concentrations (Figure S37, Supporting Information). Subsequently, in vivo PAI and PTI were performed to track the distribution of PL-CuS-in-ZIF-8 and optimize its therapeutic efficacy. For PAI analysis, A549 tumor-bearing mice were retro-orbitally injected with PL-CuS-in-ZIF-8 (10 mg kg^{-1}), and PA signals were recorded at 4, 8, 12, and 24 h post-administration. The PA signals at the tumor sites increased gradually, peaking at 12 h post-injection (Figures S38 and S39, Supporting Information), indicating effective accumulation of PL-CuS-in-ZIF-8 in the tumor. This accumulation is attributed to the EPR effect. Furthermore, at the same CuS dose, mice treated with PL-CuS-in-ZIF-8 exhibited higher PA signals compared to those treated with CuS NPs at each time point (Figure S40a, Supporting Information). Specifically, the PA signal intensity in mice treated with PL-CuS-in-ZIF-8 was approximately eight times higher than that in mice treated with CuS (Figure S40b, Supporting Information), highlighting the superior in vivo PAI capability of PL-CuS-in-ZIF-8 for tumor monitoring and therapy. Based on the time-dependent accumulation observed by PAI, thermographic images of mice were collected 12 h after retro-orbital injection. The temperature in the tumor area increased rapidly to 45 °C within 5 min, demonstrating effective hyperthermia treatment. In contrast, the temperature in the tumor region increased only slightly in the control group treated with pristine ZIF-8 (Figure S41, Supporting Information).

Encouraged by the excellent catalytic activity and photothermal capability observed in vitro, the antitumor effects of PL-CuS-in-ZIF-8 were evaluated in A549 tumor-bearing BALB/c nude mice (**Figure 4a**). When the average tumor size reached ≈13 mm^3, the tumor-bearing mice were randomly divided into six groups (five mice per group) and subjected to various treatments (G1: phosphate buffer saline (PBS), G2: PBS + laser, G3: CuS, G4: ZIF-8, G5: PL-CuS-in-ZIF-8, G6: PL-CuS-in-ZIF-8 + laser). After administering PBS and PL-CuS-in-ZIF-8 (10 mg kg^{-1}), an 808 nm laser (1 W cm^{-2}) was applied for 5 min at 12 h post-injection. During the treatment, tumors in the PBS group exhibited rapid growth. The CuS, ZIF-8, and PL-CuS-in-ZIF-8 groups showed only a slight inhibitory effect on tumor growth (Figure 4b,c). In contrast, the PL-CuS-in-ZIF-8 + laser group demonstrated significant tumor suppression, nearly eradicating the tumors (Figure 4b,c). Specifically, compared to the PBS control group, CuS treatment without laser resulted in ≈46% inhibition of tumor growth. Mice treated with PL-CuS-in-ZIF-8 and laser showed
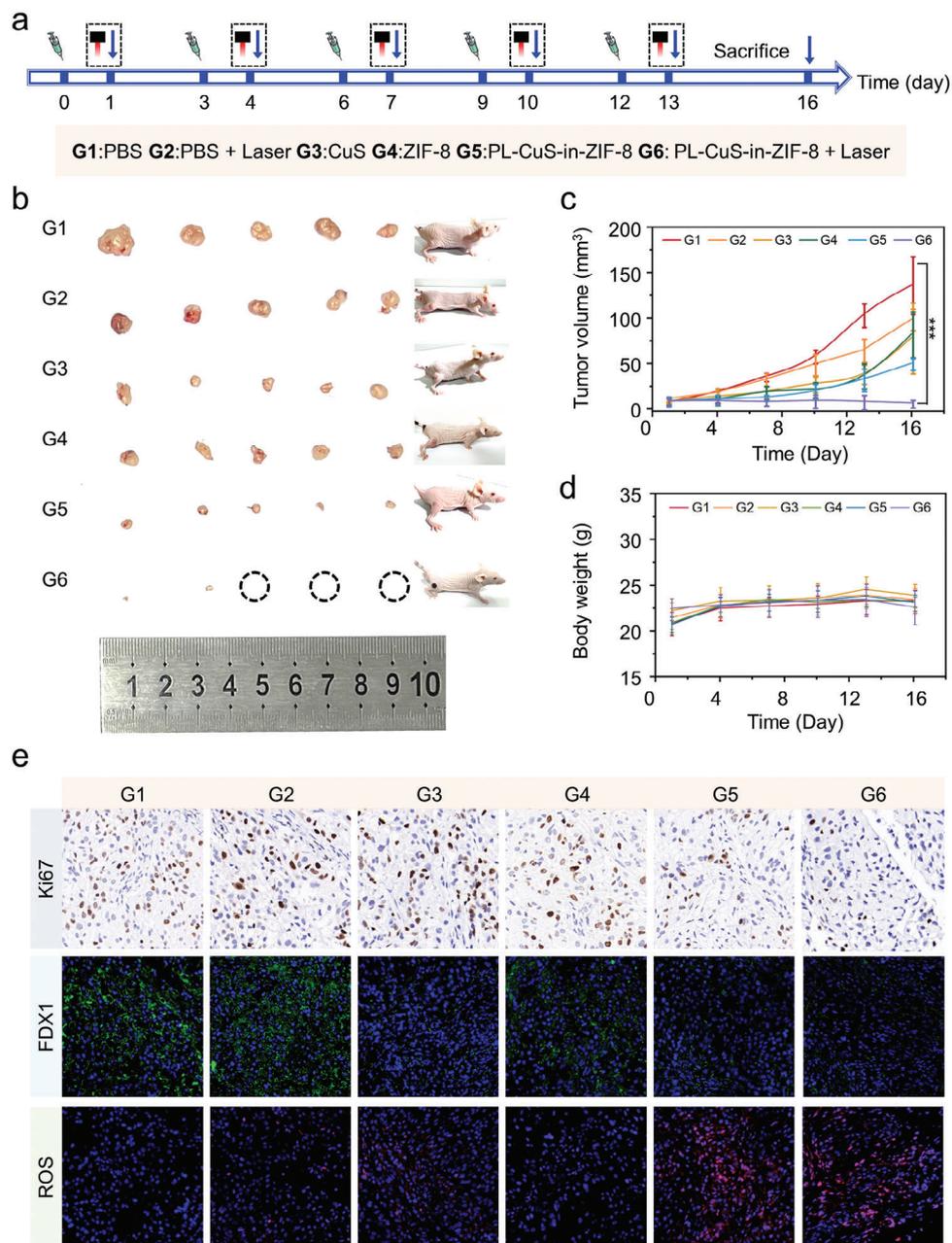
Figure 4. a) Schematic for the construction of the A549 tumor-bearing mouse model and evaluation of therapeutic efficacy. b) Photographs of tumors after 16 days of treatment. c) Tumor volumes of mice over the 16-day treatment period. d) Body weights of A549 tumor-bearing mice under different treatment conditions. e) Ki67, FDX1, and ROS staining images of tumor sections for each group. Data are shown as mean ± SD, n = 5, ***$p < 0.001$.

significantly greater suppression of tumor growth, with an inhibition rate of ≈84%. The tumor growth inhibition in the PL-CuS-in-ZIF-8 + laser group was approximately twice as high as that in the CuS NPs-treated group, suggesting that the combination of CDT and PTT using PL-CuS-in-ZIF-8 provides excellent tumor inhibition. Throughout the 16-day treatment period, no significant changes in body weight were observed in any group (Figure 4d), indicating the favorable biosafety profile of PL-CuS-in-ZIF-8.

Furthermore, a notable reduction in FDX1 expression was observed in the tumors of the PL-CuS-in-ZIF-8 + 808 nm laser

group, indicating effective induction of cuproptosis in vivo. Additionally, the tumor tissue in this group showed elevated ROS levels, which is consistent with previous results. The expression of Ki67, a marker widely used to indicate cell proliferation, was notably down-regulated in the PL-CuS-in-ZIF-8 + 808 nm laser group, reflecting strong inhibition of cell proliferation (Figure 4e). Hematoxylin and eosin (H&E) analysis of tumor tissues and major organs in various mouse groups revealed significant necrosis and apoptosis specifically in the PL-CuS-in-ZIF-8 group with NIR light irradiation, compared to other treatment groups. In contrast, the other major organs, including the liver,

2402915 (9 of 11)

heart, lungs, spleen, and kidneys, showed no apparent damage (Figure S42, Supporting Information). Moreover, all biochemical and hematological parameters remained within the normal range (Figures S43–S46, Supporting Information), further confirming the excellent biocompatibility of PL-CuS-in-ZIF-8. These results indicate that PL-CuS-in-ZIF-8 can effectively suppress tumor growth via CDT, PDT, and cuproptosis with negligible toxicity concerns.

3. Conclusion

Herein, PL-CuS-in-ZIF-8, an imaging-guided nanozyme, has been developed for tumor theranostics, demonstrating effective tumor cell elimination through its multienzymatic properties. Additionally, disruption of Cu homeostasis impacts the mitochondrial TCA cycle, leading to DLAT aggregation and Fe-S cluster protein depletion, thereby inducing cuproptosis. PL-CuS-in-ZIF-8 also exhibits superior photothermal performance, significantly improving tumor treatment efficiency. PL-CuS-in-ZIF-8—with its structural and compositional advantages—enables excellent multimodal imaging (PAI and MRI), facilitating precise tumor detection, distribution tracking, and metabolism monitoring. In tumor-bearing mouse models, PL-CuS-in-ZIF-8 effectively inhibits tumor growth with minimal side effects, and its therapeutic efficacy is further enhanced by laser irradiation. This strategy presents a promising approach for precise imaging-guided tumor therapy using nanozymes.

4. Experimental Section

Preparation of PL-CuS-in-ZIF-8 NPs: First, $Zn(OAc)_2 \cdot 2H_2O$ (220 mg) was dissolved in methanol (50 mL). Subsequently, 2-methylimidazole (656 mg) and CuS NPs were mixed in methanol (50 mL), followed by the addition of the $Zn(OAc)_2 \cdot 2H_2O$ methanol solution. After stirring for 3 h, the mixture was kept at room temperature and atmospheric pressure for 24 h. The PL-CuS-in-ZIF-8 NPs were obtained by centrifugation (10 000 rpm, 5 min), washed three times with methanol, and the resulting green powder was dried at 50 °C overnight.

Hyperpolarized ^{129}Xe NMR: The gas mixture was polarized using a custom-built hyperpolarizer and then bubbled directly into a 10 mm NMR tube containing the MOF sample for 15 s, followed by a 3 s delay to allow the bubbles to collapse. The ^{129}Xe spectra were acquired using a zg pulse sequence (rectangular pulse, pulse length p1 = 31.8 ms).

Hyper-CEST Spectrum: The hyperpolarized gas mixture was introduced into a 10 mm NMR tube for 20 s, which was followed by a 3 s delay to let the bubbles collapse. The ^{129}Xe NMR spectra were acquired after the Xe within the ZIF-8 was saturated by a continuous-wave pulse (6.5 μT, 10 s). All the ^{129}Xe NMR spectra were acquired in a single scan and processed using Lorentzian broadening (LB = 5 Hz).

Hyper-CEST MRI: Images were obtained using a RARE sequence (slice thickness = 30 mm, field of view = 30 mm × 30 mm, matrix size = 32 × 32, in-plane resolution = 0.9375 mm × 0.9375 mm, bandwidth = 5400 Hz, echo time = 4.97 ms, repetition time = 28 080 ms, centric k-space encoding, no partial Fourier transform acceleration, RARE factor = 8). Sixteen on-resonant and sixteen off-resonant scans were acquired and averaged. For each excitation, after the hyperpolarized ^{129}Xe bubbled into the solution for 20 s, a 3 s delay was incorporated to allow the bubbles to collapse. Before acquiring the image, the saturation pulse (13 μT, 5 s) was applied to saturate the on-resonant (−109.5 ppm, relative to dissolved Xe in solution at 0 ppm) or off-resonant (109.5 ppm, relative to dissolved Xe in solution at 0 ppm). The magnetic resonance images were

processed using MATLAB (R2014a; MathWorks), with the 32 × 32 image matrix interpolated into a 128 × 128 image matrix. The Hyper-CEST effect for on-resonant saturation was analyzed in comparison to off-resonant saturation for each pixel, using the formula (CEST effect = (Intensity$_{off}$ − Intensity$_{on}$)/Intensity$_{off}$) on a point-by-point basis.

In Cell Singlet Oxygen Detection: DCFH-DA was used as a fluorescent probe for detecting ROS to reflect oxidative stress triggered by PL-CuS-in-ZIF-8. In brief, A549 cells were treated with either PL-CuS-in-ZIF-8 (100 μg mL^{-1}) or ZIF-8 (100 μg mL^{-1}) for 2 h. After incubation, the medium was removed, and the cells were washed thrice with PBS (pH 7.4). Subsequently, the cells were stained with DCFH-DA (10 μM) for 30 min, followed by capturing fluorescence images using a Nikon A1R/A1 confocal laser scanning microscope.

Animals and Tumor Model: All animal procedures were conducted in strict accordance with the Guideline for Animal Care and Use, Innovation Academy for Precision Measurement Science and Technology, Chinese Academy of Sciences (APM21013T). Healthy male BALB/c mice (3–4 weeks) were provided by Hubei Beiente Biotech Co., Ltd. (Wuhan, China). The A549 cells (1.5×10^6) were suspended in PBS (0.1 mL) and subcutaneously injected into the right hind leg of the BALB/c nude mouse to establish the tumor model.

In Vivo PA Imaging: Five nude mice were administered a 200 μL orbital venous plexus injection of PL-CuS-in-ZIF-8 NPs (200 mg mL^{-1}). At 1, 4, 8, 12, 24, and 48 h post-injection, the mice underwent PA imaging using the MSOT inVision 256-TF small animal imaging system (iThera Medical GmbH, Munich, Germany).

In Vivo Photothermal Imaging: Mice with A549 tumors were randomly assigned to three groups (n = 5 per group). Each group received an orbital venous plexus injection of either PBS, ZIF NPs, or PL-CuS-in-ZIF-8 NPs. At each predetermined time point, an 808 nm laser (1 W cm^{-2}, 5 min) was applied to the tumor sites. Photothermal images of anesthetized mice were then collected using a thermal camera to record temperature changes.

In Vivo Therapy: Mice with A549 tumors were randomly assigned to six groups (n = 5 per group). Each group received an orbital venous plexus injection of one of the following treatments: 1) PBS, 2) PBS + laser, 3) ZIF NPs, 4) ZIF-8 NPs + laser, 5) PL-CuS-in-ZIF-8 NPs, or 6) PL-CuS-in-ZIF-8 NPs + laser. At 12 h post-injection, the tumor sites of the mice in the laser-treated groups were exposed to NIR light (808 nm, 1 W cm^{-2}, 5 min) for photothermal therapy. NIR exposure was repeated every 2 days for a duration of 16 days. Tumor volume (V) was determined using the following formula.

$$V = \frac{L \times W^2}{2} \tag{1}$$

The shortest and longest tumor diameters are denoted by W and L, respectively. The body weight and tumor volumes of the mice were assessed every two days throughout the study. Following a 16-day treatment period, the mice were sacrificed, and their organs along with the tumors were removed. Subsequently, these tissues were subjected to histological examination through H&E staining to evaluate any alterations in the tissue structure.

Statistical Analysis: Data are expressed as mean ± standard deviation from at least three independent replicates. Statistical analysis was conducted using one-way analysis of variance (ANOVA), complemented by Tukey's post hoc test for multiple comparisons, all performed within OriginPro 2021. Significance levels are indicated by asterisks: a p-value of less than 0.05 is the benchmark for statistical significance, ** for $p < 0.01$, and *** for $p < 0.001$.

Supporting Information

Supporting Information is available from the Wiley Online Library or from the author.

**ADVANCED
SCIENCE NEWS**

www.advancedsciencenews.com

**ADVANCED
HEALTHCARE
MATERIALS**

www.advhealthmat.de

Conflict of Interest

The authors declare no conflict of interest

Data Availability Statement

The data that support the findings of this study are available in the supplementary material of this article.

[1] S. Solier, S. Müller, T. Cañeque, A. Versini, A. Mansart, F. Sindikubwabo, L. Baron, L. Emam, P. Gestraud, G. D. Pantos, *Nature* **2023**, *617*, 386.

[2] E. J. Ge, A. I. Bush, A. Casini, P. A. Cobine, J. R. Cross, G. M. DeNicola, Q. P. Dou, K. J. Franz, V. M. Gohil, S. Gupta, *Nat. Rev. Cancer* **2022**, *22*, 102.

[3] J. Guo, J. Cheng, N. Zheng, X. Zhang, X. Dai, L. Zhang, C. Hu, X. Wu, Q. Jiang, D. Wu, H. Okada, P. P. Pandolfi, W. Wei, *Adv. Sci.* **2021**, *8*, 2004303.

[4] N. M. Garza, A. B. Swaminathan, K. P. Maremanda, M. Z. Fli, V. M. Gohil, *Trends Endocrinol. Metab.* **2023**, *34*, 21.

[5] F. Zhao, L. Liang, H. Wang, C. Wang, D. Su, Y. Ying, W. Li, J. Li, J. Zheng, L. Qiao, *Adv. Funct. Mater.* **2023**, *33*, 2300941.

[6] W. Xie, Z. Guo, L. Zhao, Y. Wei, *Prog. Mater Sci.* **2023**, *138*, 101145.

[7] W. Wang, W. Mo, Z. Hang, Y. Huang, H. Yi, Z. Sun, A. Lei, *ACS Nano* **2023**, *17*, 19581.

[8] H. Tian, J. Duan, B. Li, S. Qin, E. C. Nice, W. Zhang, T. Lang, H. Zhang, C. Huang, *Adv. Funct. Mater.* **2023**, *33*, 2306584.

[9] Y. Ruan, H. Zhuang, X. Zeng, L. Lin, X. Wang, P. Xue, S. Xu, Q. Chen, S. Yan, W. Huang, *Adv. Healthcare Mater.* **2023**, *13*, 2302537.

[10] L. Qiao, G. Zhu, T. Jiang, Y. Qian, Q. Sun, G. Zhao, H. Gao, C. Li, *Adv. Mater.* **2023**, *36*, 2308241.

[11] B. Guo, F. Yang, L. Zhang, Q. Zhao, W. Wang, L. Yin, D. Chen, M. Wang, S. Han, H. Xiao, *Adv. Mater.* **2023**, *35*, 2212267.

[12] W. Chen, W. Xie, Z. Gao, C. Lin, M. Tan, Y. Zhang, Z. Hou, *Adv. Sci.* **2023**, *10*, 2303694.

[13] Y. Xu, S. Y. Liu, L. Zeng, H. Ma, Y. Zhang, H. Yang, Y. Liu, S. Fang, J. Zhao, Y. Xu, *Adv. Mater.* **2022**, *34*, 2204733.

[14] S. Li, L. Bu, L. Cai, *Signal Transduct. Target. Ther.* **2022**, *7*, 158.

[15] L. Chen, J. Min, F. Wang, *Signal Transduct. Target. Ther.* **2022**, *7*, 378.

[16] P. Yu, X. Zhang, N. Liu, L. Tang, C. Peng, X. Chen, *Signal Transduct. Target. Ther.* **2021**, *6*, 128.

[17] B. A. Carneiro, W. S. El-Deiry, *Nat. Rev. Clin. Oncol.* **2020**, *17*, 395.

[18] B. R. Stockwell, *Cell* **2022**, *185*, 2401.

[19] P. Tsvetkov, S. Coy, B. Petrova, M. Dreishpoon, A. Verma, M. Abdusamad, J. Rossen, L. Joesch-Cohen, R. Humeidi, R. D. Spangler, J. K. Eaton, E. Frenkel, M. Kocak, S. M. Corsello, S. Lutsenko, N. Kanarek, S. Santagata, T. R. Golub, *Science* **2022**, *375*, 1254.

[20] F. Liu, C. Guo, X. Li, Y. Li, S. Xu, T. D. James, L. Wang, *Nano Today* **2024**, *54*, 102116.

[21] Y. Zhang, S. Yang, J. Wang, Y. Cai, L. Niu, X. Liu, C. Liu, H. Qi, A. Liu, *Talanta* **2021**, *233*, 122594.

[22] Q. Bai, M. Liang, W. Wu, C. Zhang, X. Li, M. Liu, D. Yang, W. W. Yu, Q. Hu, L. Wang, *Adv. Funct. Mater.* **2022**, *32*, 2112683.

[23] S. Wang, Y. Pang, S. Hu, J. Lv, Y. Lin, M. Li, *Chem. Eng. J.* **2023**, *451*, 138864.

[24] Z. Zhan, W. Zeng, J. Liu, L. Zhang, Y. Cao, P. Li, H. Ran, Z. Wang, *ACS Appl. Mater. Interfaces* **2023**, *15*, 24071.

[25] M. Su, Z. Wu, T. Yan, N. Li, X. Li, T. Hou, J. Liu, C. Zhang, C. Zhu, Z. Wang, J. Zhang, *Adv. Funct. Mater.* **2024**, 2409580, https://doi.org/10.1002/adfm.202409580.

[26] Z. Zhang, J. Wen, J. Zhang, D. Guo, Q. Zhang, *Adv. Healthcare Mater.* **2023**, *12*, 2201746.

[27] F. Gao, L. Zhu, L. Jiang, J. Zhang, S. Ji, W. Gao, G. Ma, Y. Chang, X. Ma, Y. Guo, *Adv. Funct. Mater.* **2024**, *34*, 2312182.

[28] X. Meng, Z. Liu, Y. Cao, W. Dai, K. Zhang, H. Dong, X. Feng, X. Zhang, *Adv. Funct. Mater.* **2017**, *27*, 1605592.

[29] M. Xia, Q. Wang, Y. Liu, C. Fang, B. Zhang, S. Yang, F. Zhou, P. Lin, M. Gu, C. Huang, *Nat. Commun.* **2024**, *15*, 460.

[30] Z. Wang, X. Tang, X. Wang, D. Yang, C. Yang, Y. Lou, J. Chen, N. He, *Chem. Commun.* **2016**, *52*, 12210.

[31] G. Cai, P. Yan, L. Zhang, H.-C. Zhou, H.-L. Jiang, *Chem. Rev.* **2021**, *121*, 12278.

[32] R. F. Mendes, F. Figueira, J. P. Leite, L. Gales, F. A. Almeida Paz, *Chem. Soc. Rev.* **2020**, *49*, 9121.

[33] R. V. Jagadeesh, K. Murugesan, A. S. Alshammari, H. Neumann, M.-M. Pohl, J. Radnik, M. Beller, *Science* **2017**, *358*, 326.

[34] M. Ding, R. W. Flaig, H.-L. Jiang, O. M. Yaghi, *Chem. Soc. Rev.* **2019**, *48*, 2783.

[35] K. Suresh, A. J. Matzger, *Angew. Chem., Int. Ed.* **2019**, *58*, 16790.

[36] Q. Wang, D. Astruc, *Chem. Rev.* **2019**, *120*, 1438.

[37] R. Freund, O. Zaremba, R. Arnauts, R. Ameloot, M. Skorupskii, M. Dincǎ, A. Bavykina, J. Gascon, A. Ejsmont, J. Goscianska, *Angew. Chem., Int. Ed.* **2021**, *60*, 23975.

[38] R. Wang, M. Qiu, L. Zhang, M. Sui, L. Xiao, Q. Yu, C. Ye, S. Chen, X. Zhou, *Adv. Mater.* **2023**, *35*, 2306748.

[39] S. Liang, X. Xiao, L. Bai, B. Liu, M. Yuan, P. a. Ma, M. Pang, Z. Cheng, J. Lin, *Adv. Mater.* **2021**, *33*, 2100333.

[40] W. Jiang, H. Zhang, J. Wu, G. Zhai, Z. Li, Y. Luan, S. Garg, *ACS Appl. Mater. Interfaces* **2018**, *10*, 34513.

[41] Q. Zhou, Q. Rao, H. Li, M. Zhang, X. Zhao, L. Shi, C. Ye, X. Zhou, *Magn. Reson. Lett.* **2021**, *1*, 2.

[42] Q. Zeng, Q. Bie, Q. Guo, Y. Yuan, Q. Han, X. Han, M. Chen, X. Zhang, Y. Yang, M. Liu, *Proc. Natl. Acad. Sci. USA* **2020**, *117*, 17558.

[43] M. Tang, J. Ni, Z. Yue, T. Sun, C. Chen, X. Ma, L. Wang, *Angew. Chem., Int. Ed.* **2024**, *63*, e202315031.

[44] Y. Wang, L. Zhang, F. Zhou, *Cell. Mol. Immunol.* **2022**, *19*, 867.

[45] L.-S. Lin, T. Huang, J. Song, X.-Y. Ou, Z. Wang, H. Deng, R. Tian, Y. Liu, J.-F. Wang, Y. Liu, G. Yu, Z. Zhou, S. Wang, G. Niu, H.-H. Yang, X. Chen, *J. Am. Chem. Soc.* **2019**, *141*, 9937.